Effects of Electrojet Turbulence on a Magnetosphere-Ionosphere Simulation of a Geomagnetic Storm

M. Wiltberger, [1] **V. Merkin,** [2] **B. Zhang,** [1] **F. Toffoletto,** [3] **M. Oppenheim,** [4] **W. Wang,** [1] **J. G. Lyon,** [5] **J. Liu,** [1] **Y Dimant,** [4] **M. I. Sitnov,** [2] **and G. K. Stephens** [2]

[1] High Altitude Observatory, National Center for Atmospheric Research, Boulder, Colorado, USA.
[2] Applied Physics Laboratory, Johns Hopkins University, MD, USA.
[3] Department of Physics and Astronomy, Rice University, TX, USA.
[4] Center for Space Physics, Boston University, Boston, Massachusetts, USA
[5] Department of Physics and Astronomy, Dartmouth College, Hanover, NH, USA.

Key Points:

- A methodology for including Anomalous Electron Heating (AEH) and Nonlinear Current (NC) enhancements to ionospheric conductance is developed.
- Inclusion of AEH and NC affects reduces cross polar cap potential and improves agreement with DMSP observations.
- Higher inner magnetospheric pressures are also seen when AEH and NC affects are included improving agreement with D_{ST} and empirical models

Corresponding author: M. Wiltberger, `wiltbemj@ucar.edu`

Abstract

Ionospheric conductance plays an important role in regulating the response of the magnetosphere-ionosphere system to solar wind driving. Typically models of magnetosphere-ionosphere coupling include changes to ionospheric conductance driven by EUV ionization and electron precipitation. Anonomlous electron heating and non-linear current effects of the Farley-Bunemman instability can also create significant enhancements to the ionospheric conductance, especially in electrojets. We have implemented a method of including electrojet turbulence (ET) affects into the ionospheric conductance model utilized within geospace simulations. Our particular implementation is tested with simulations of the coupled Lyon-Fedder-Mobarry global magnetosphere model with the Rice Convection Model of the inner magnetosphere. We examine the impact of including ET modified conductances in a case study of the geomagnetic storm that occurred on 17 March 2013. Simulations with ET show a 13 % reduction in the cross-polar-cap potential at the beginning of the storm and up to 20 % increases in the Hall conductance. These simulation results show better agreement with Defense Meteorological Satellite Program (DMSP) observations, including capturing features of sub-auroral polarization streams. The field aligned current (FAC) patterns show little differences during the peak of storm and agree well with Active Magnetosphere and Planetary Electrodynamics Response Experiment (AMPERE) reconstructions. Typically the simulated FACs are stronger and at slightly higher latitudes than shown by the AMPERE observations. The inner magnetospheric pressures derived from Tsyganeko empirical magnetic field model show that the inclusion of the ET effects increases the peak pressure and bring the results into better agreement with the empirical model.

1 Introduction

The role of ionospheric conductivity in the solar wind-magnetosphere-ionosphere coupling has been recognized for a long time [e.g., *Coroniti and Kennel*, 1973; *Hill et al.*, 1976]. The conductivity allows closure of field-aligned Birkeland currents generated in the magnetosphere and governs the amount and distribution of energy dissipation (Joule heating) in the ionosphere. Due to this current closure, the height-integrated conductivity or ionospheric conductance exerts feedback on the global magnetosphere affecting such distant regions as the magnetopause and the bow shock [*Merkine et al.*, 2003; *Merkin et al.*, 2005a,b]. Since the conductance is a tensor relating currents and electric fields [e.g., *Kelley*, 1989, p. 45] for a given distribution of the field-aligned currents (FACs), it determines the ionospheric plasma convection and, thus, due to at least partial mapping of electric fields between the ionosphere and magnetosphere, the magnetospheric plasma convection as well. This conjecture underlies most models of magnetospheric convection that include magnetosphere-ionosphere (MI) coupling [*Wolf*, 1983; *Fedder et al.*, 1995a; *Raeder et al.*, 1995; *Ridley et al.*, 2004; *Merkin and Lyon*, 2010]. Effects of the ionospheric conductance on the magnetosphere have been mainly reported using global magnetosphere (MHD) simulations, and due to many modeling results it has become rather clear that the ionospheric conductance may be a significant factor controlling the global magnetosphere behavior. For instance, ionospheric conductance appears as a parameter governing passively [*Siscoe et al.*, 2002a,b] or actively [*Merkine et al.*, 2003; *Merkin et al.*, 2005b] the saturation of the cross-polar cap potential in global models through regulation of the FAC strength. *Ridley et al.* [2004] considered in detail effects of different contributions to the ionospheric conductance, including solar illumination and magnetospheric particle precipitation. The latter, in particular, was also shown to have a major effect on the initiation of substorms in global models [*Raeder et al.*, 2001].

Despite these modeling results, observational evidence for conductance effects on the magnetosphere remains scarce due primarily to the notorious difficulty of directly measuring the ionospheric conductivity, let alone conductance. Nevertheless, *Ohtani et al.* [2014] was able to show statistically that the ionospheric FACs depend on the level of the solar irradiance, measured by the F10.7 flux, and thus on the dayside ionospheric conductance. Notably, not only the dayside, but also the nightside, currents responded in the same way to solar cycle variations of the F10.7 flux, i.e., their intensity increased with enhanced solar activity. *Ohtani et al.* [2014] noted that

this had significant implications for the global structure of the magnetosphere and the energy and momentum exchange between the solar wind and the magnetosphere.

Conductivity of the ionospheric plasma is typically assumed to be produced by the Extreme Ultraviolet (EUV) solar radiation and by magnetospheric particle precipitation [*Rasmussen et al.*, 1988; *Moen and Brekke*, 1993]. These are the processes that are typically included in the calculation of ionospheric convection by magnetospheric models [*Fedder et al.*, 1995b; *Janhunen*, 1996; *Toffoletto et al.*, 2003; *Raeder*, 2003; *Wiltberger et al.*, 2009]. However, there are other processes in the ionospheric plasma that can create conductivity but are usually completely ignored in magnetospheric models, e.g., the ionospheric E layer micro-turbulence [*Dimant and Oppenheim*, 2011a,b]. During active geomagnetic events, such as magnetic storms, strong DC convection electric fields create the high-latitude electrojets in the E-region ionosphere between 90 and 125 km altitude. These fields drive plasma instabilities, mainly the Farley-Buneman (FB) instability [*Buneman*, 1963; *Farley*, 1963]. They generate plasma turbulence that consists of electrostatic field fluctuations coupled to plasma density irregularities [*Balsley and Farley*, 1971; *Cohen and Bowles*, 1967; *Crochet et al.*, 1979; *Kudeki et al.*, 1987; *Fukao et al.*, 1998; *Pfaff et al.*, 1987; *Rose et al.*, 1992]. Typical wavelengths of E-region turbulence are between tens of centimeters and tens of meters, while characteristic wave periods are a few milliseconds. This turbulence modifies the ionospheric conductivities in two ways: (1) It causes Anomalous Electron Heating (AEH), raising the temperatures from between 300 to 500 K up to 4000 K [*Bahcivan*, 2007; *Foster and Erickson*, 2000; *Providakes et al.*, 1988; *Schlegel and St Maurice*, 1981; *St Maurice*, 1990; *Stauning and Olesen*, 1989] (2) It drives Nonlinear Currents (NC) that enhance the ion-dominated Pedersen conductivity [*Buchert et al.*, 2006; *Dimant and Oppenheim*, 2011c,d; *Oppenheim*, 1997; *Oppenheim and Dimant*, 2013; *Rogister and Jamin*, 1975].

AEH occurs when the FB instability creates small turbulent electric field component along B [*Providakes et al.*, 1988; *St Maurice and Laher*, 1985; *St Maurice*, 1990]. This means that only 3-D models and simulations can evaluate it. A model of AEH that uses the RMS turbulent electric field and density fluctuations and takes into account a feedback of the electron and ion temperature modifications on the threshold electric field has been developed [*Dimant and Milikh*, 2003; *Milikh and Dimant*, 2002, 2003]. Model results showed good agreement with radar measurements of AEH [*Milikh and Dimant*, 2003]. Strong electron temperature elevations caused by AEH do not affect the ionospheric conductivity directly because the Pedersen current is carried largely by ions, while the Hall current, carried mainly by electrons, is almost temperature-independent. However, local AEH increases E-region electron density due to a partial suppression of the electron-ion recombination rate through electron temperature elevation [*Dimant and Milikh*, 2003; *Gurevich*, 1978; *Milikh and Dimant*, 2003; *Milikh et al.*, 2006; *Schlegel*, 1982; *St Maurice*, 1990]. This effect was verified with detailed radar observations [*Milikh et al.*, 2006].

E-region turbulence also gives rise to the direct non-linear current carried mostly by electrons in the Pedersen direction, as explained in *Dimant and Oppenheim* [2011c]. The NC increases the entire macro-scale current, enhancing the total plasma conductivity, especially the crucial Pedersen component as explained in *Dimant and Oppenheim* [2011d] The direct NC develops simultaneously with the turbulence, i.e., almost instantaneously, and reaches a similar amplitude to the laminar Pedersen current carried by the ions. Unlike the AEH, the NC directly increases the Pedersen conductivity. The NC will change the ionospheric current closure, Joule heating, and cross-polar cap potential pattern.

An initial effort to include effects of the electrojet turbulence in a global magnetosphere simulation was made by *Merkin et al.* [2005b]. They modified the ionospheric conductance module within the Lyon-Fedder-Mobarry (LFM) global magnetosphere model by including only the AEH contribution in the conductance calculation. A simplified AEH model was used whereby the classical conductance tensor components were multiplied by a factor that scaled roughly as $\propto \sqrt{E}$, where E is the convective electric field, in regions where $E > 20$ mV/m was satisfied. This dependence approximated well the numerical results by *Milikh and Dimant* [2003] based on the heuristic model of the turbulent electric field by *Dimant and Milikh* [2003]. *Merkin et al.* [2005b] found that the inclusion of this significant source of increased conductivity led to a sub-

stantial reduction of the strength of ionospheric convection and a much better agreement with the corresponding observations during the Halloween 2003 geomagnetic storm.

Since the turbulence theory relied on the specification of the background ionosphere and thermosphere, including plasma densities and collision rates, *Merkin et al.* [2005b] used simplified parametric dependencies of the turbulent correction to the conductance as a function of the convective electric field. They noted that a more self-consistent approach would be to incorporate anomalous electron heating and cooling into a first-principles ionosphere-thermosphere model which would then use that information for improved energy balance. Such an effort has recently been undertaken by *Liu et al.* [2016] who included these effects in the thermosphere-ionosphere electrodynamics global circulation model (TIEGCM). As a result, they obtained a significant increase in the E region electron temperature in the auroral oval and the polar cap of up to a factor of 4, and an increase in Pedersen conductivity of up to 88% relative to the background values without the turbulent corrections.

The ultimate goal of our modeling effort is to combine the improved TIEGCM model with turbulent corrections, including the NC effects, with the LFM global magnetosphere simulations to study global scale effects of ionospheric turbulence. In the present paper, we take a step in that direction although here we do not yet use LFM coupled with TIEGCM. Instead, we implement a parameterized model of the E layer turbulence that is more advanced then the one used by *Merkin et al.* [2005b], in particular, including both AEH and NC effects. This model is then used within the Magnetosphere-Ionosphere Coupler/Solver (MIX) code [*Merkin and Lyon*, 2010] which drives ionospheric convection and specifies the inner boundary condition in the LFM model.

We also employ the version of LFM that is coupled with the Rice Convection Model (RCM) *Pembroke et al.* [2012], which is necessary for storm time simulations. Since the inclusion of a stronger ring current pressure leads to increased Region 2 FACs, this affects the current closure in the ionosphere and, in particular, redistributes plasma convection and electric fields from the polar cap more into the electrojets. This, in turn, spatially relocates the regions where the turbulence corrections operate, since that is modulated by the intensity of the convective electric field. These effects, enabled by the inclusion of the RCM model into the global calculations, were missing in our previous, less advanced simulations [*Merkin et al.*, 2005b].

Other modeling groups have coupled inner magnetosphere models such as the RCM to global MHD simulations for simulating the magnetosphere during storms. *De Zeeuw et al.* [2004] did the initial work coupling the RCM with the BATS-R-US magnetosphere solution.*Welling and Ridley* [2010] conducted a validation study of the Space Weather Modeling Framework (SWMF) with the RCM coupled to the the BAT-S-RUS MHD magnetosphere model and found good agreement with inner magnetosphere pressures and magnetic field. *Raeder et al.* used a coupled model that consisted of the OpenGGCM global MHD model, the RCM inner magnetosphere model, and the CTIM ionosphere-thermosphere model to simulate the March 17, 2013 geomagnetic storm, which is known to have developed SAPS. They found that the model reproduced many of the salient features of SAPS, such as the strong northward fields and associated ion drifts, as well as the trough in electron density.

The goal of this paper is to explore the effects of ionospheric small-scale electrojet turbulence (ET) on the global structure of the magnetosphere and ionosphere using the LFM-RCM global simulation tool. In particular, we are going to examine the effects of the saturated FB instability through both the NC and then AEH. The FB instability occurs at high latitudes when the $\vec{E} \times \vec{B}$ speed exceeds the ion acoustic speed by a small amount. We chose the geomagnetic storm of 17 March 2013 as a testbed for these simulations since it was a recent modest storm with both solar wind measurements and a broad range of observations. This allows us to validate the results of including the effects of ET on the simulation results.

This paper is organized as follows. We begin with a detailed discussion of the LFM-RCM model and the inclusion of the ET effects in Section 2. This section finishes with an overview of the 17 March 2013 solar wind conditions and details of the simulation setup. Section 2.3 presents

the simulation results for the runs with and without the ET implementation and compares the results with Defense Meteorological Satellite Program (DSMP) and Active Magnetosphere and Planetary Electrodynamics Response Experiment (AMPERE) observations. It also compares inner magnetosphere pressures with an empirical model. We finish the paper with a brief discussion of the results and next steps for the research efforts using this new modeling capability.

2 Simulation Setup

This study focuses on using the geomagnetic storm that occurred on 17 March 2013 as a case study for two new features of the LFM-RCM geospace model. As previously discussed the LFM-RCM model combines the Lyon-Fedder-Mobarry MHD model of the magnetosphere with the Rice Convection Model of the inner magnetosphere and the Magnetosphere-Ionosphere Coupler Solver of ionospheric electrodynamics to provide a coupled model of the geospace system. *Pembroke et al.* [2012] describes in detail the basic process of coupling these three models together during idealized solar wind conditions with modest solar wind driving and no dipole tilt. Section 2.1 describes how this approach has been modified to include realistic solar wind conditions, including nonzero IMF B_Y, as well as variations in the Earth's dipole tilt. *Merkin et al.* [2005b] implemented an adjustment to the ionospheric conductances based upon the theoretical analysis of the FB instability conducted by *Dimant and Milikh* [2003]. This capability has not been widely used in LFM simulations, but is being made part of the LFM-RCM geospace model. Section 2.2 discusses how both the anomalous electron heating and nonlinear current aspects of the electrojet turbulence are implemented in the MIX portion of the LFM-RCM model. Next we present the results of simulations for a geomagnetic storm that occurred on 17 March 2013. We compare and contrast the results of LFM-RCM simulations with and without the Electrojet Turbulence including comparisons with a range of observations. The final section of the paper we discuss our results and next steps.

2.1 LFM-RCM

Pembroke et al. [2012] provides a detailed description of the coupling process between the LFM, MIX and RCM models for simulations of geospace. Since that study used idealized solar wind conditions with no dipole tilt after reviewing the basics of the LFM-RCM coupling this section will address the changes made to coupling infrastructure needed to allow model to work for realistic solar wind conditions and dipole tilts.

The fundamental aspect of coupling these models is an exchange of magnetic field and plasma information in the inner magnetosphere to RCM from LFM and then an update of the plasma information from RCM to the LFM. The MIX model is providing ionospheric potential information to both the LFM and RCM models. All of the exchanges use the Center for Integrated Space Weather Modeling (CISM) coupling infrastructure and that infrastructure is utilized in the update version [*Goodrich et al.*, 2004]. To transfer information from the LFM to the RCM the LFM computes time averages of the pressure, density and magnetic field over an exchange interval. The averaged fields are interpolated onto an intermediate regular Cartesian grid. This intermediate grid is then used to calculate field line-averaged pressure and density for positions on the RCM's ionospheric grid. A key innovation of the *Pembroke et al.* [2012] was the implementation of the plasma-β methodology for setting the location of the outer boundary of the RCM. This switch, which essentially prevented the RCM from computing regions with large flows, remains active in the storm simulations we present in this paper. After the RCM computes its plasma pressures and densities these values are transferred back to the LFM once again using the intermediate grid. The RCM density model includes a modification to a fit of the *Gallagher et al.* [2000] plasmasphere model. At this time we have not implemented a dynamic plasmasphere calculation, but that is logical next step for improvement of the coupled model. Another set of field line traces from the RCM ionospheric grid points are used to determine the local values on intermediate grid and than those values are interpolated to LFM grid points. The mapping back to LFM assumes that the distribution of plasma density and pressure is constant along field lines. As be-

fore, the RCM values do not immediately replace the LFM values, instead they are slowly bled into the LFM over the exchange time interval. It is important to note that the previous work used a 1-minute exchange interval as a balance between speed and accuracy. For strong solar wind driving conditions we have found it necessary to reduce the coupling interval to 15-seconds in order ensure stability and prevent the coupled model from producing unrealistically large electric fields in the inner magnetosphere.

The first major modification to the previous coupling efforts is in support of including dipole tilts in the calculation of the coupled model. The LFM-MIX model has long had support for conducting simulations with realistic dipole tilts. This is done by having dipole axis of the Earth aligned with the Z-axis of the computational model and inputing the solar wind conditions in SM coordinates. As *Hapgood* [1992] explains the SM coordinate system has the Z-axis parallel to the north magnetic pole and transformation between this coordinate system and the more commonly used GSM coordinate system is simply rotation about the Y-axis by the dipole tilt angle. The cartesian intermediate grid is setup in SM coordinates for the transfer of data to and from the LFM to RCM the ionospheric foot points are transformed from geographic coordinates to SM coordinates using the GEOPACK coordinate transform package. The RCM typically includes the effects of the corotation potential which is not part of stand alone LFM-MIX, but is enabled when coupled with the RCM.

The second key modification of the LFM-RCM coupling is how the asymmetries in the ionosphere are addressed. In the MIX module the ionospheric potential for the northern and southern hemispheres are calculated independently. The field-aligned current patterns taken from the global MHD simulation are computed for each hemisphere independently and the ionospheric conductances can be different. The first major difference in the conductance comes from the implementation of a EUV conductance model that calculates the local value of the Hall and Pedersen conductance based upon the solar zenith angle and the F107 flux value. We have adapted the approach used by Assimilative Mapping of Ionospheric Electrodynamics (AMIE) for the MIX module [*Richmond*, 1992] for the calculation of the EUV conductance. The ionospheric conductance model also includes an empirical model for electron precipitation. As described by *Wiltberger et al.* [2009] this model includes modifications of the precipitation values based upon the local EUV conductance values allowing the model to simulate seasonal variations of particle precipitation and their impacts on geospace system. On the other hand the RCM is a 2D model which eliminates the field-aligned dimension from the calculation and only requires setting the potential in one hemisphere.

The solution we have adopted for the version of the coupled simulations presented here works as follows. The low latitude boundary of the ionospheric solution for the electrodynamic solver is extended equatorward from 45° to 60° colatitude. The 45° boundary corresponds to dipole mapping of the 2 R_E inner boundary of the MHD solution grid within the LFM. For the northern hemisphere, the typical low latitude boundary condition of assuming that potential is zero is used. In the RCM the low latitude boundary is at 75° colatitude, and in the region between the MIX lower boundary and the RCM lower boundary the RCM electric field is set to zero. The northern hemispheric values for the potential, as well as the average energy and flux of precipitating electrons, are then stored for latter passage to the RCM for its calculation. The computation of the southern hemisphere potential is done poleward of 45° colatitude with the boundary value being set by the potential obtained from the northern hemisphere at that location. By setting the southern hemisphere boundary with the northern hemisphere values, we ensure the potentials from each hemisphere match when mapped to the equatorial plane allowing for a stable evolution of the coupled model.

2.2 Electrojet Turbulence Implementation

Dimant and Oppenheim [2011b] developed a model of how FB instability modifies E-region conductivities when driven by strong DC electric fields. This instablity gives rise to both nonlinear currents and anomalous electron heating. Both these will increase the conductivities. This
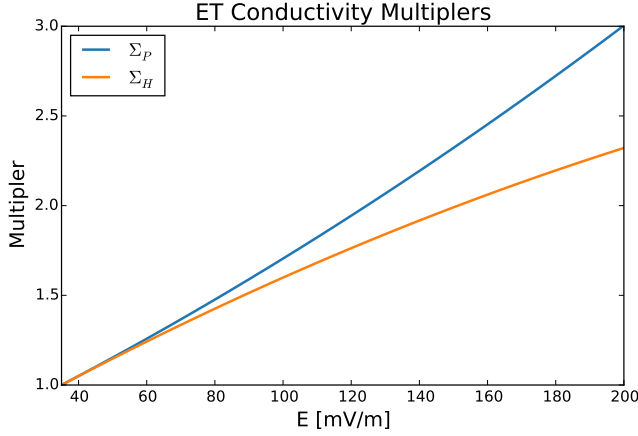
Figure 1. The conductivity multipliers for the Electrojet Turbulence effects. The blue curve is for the Pedersen conductance while the orange curve is for the Hall conductance. The effects occur for all values above 35 mV/m.

model was incorporated into the MIX module as a set of conductance correction factors that depend on the driving electric field.

The model of AEH was developed in *Dimant and Milikh* [2003] assuming a specific FB instability level. This self-consistent approach accounts for the fact that as the FB instability raises the electron temperature T_e, it increases the instability threshold field, $E_{\text{Thr}}^{\min}$, causing the saturated turbulence level to grow with E_0 much more slowly than if T_e were constant. It also accounts for kinetic modification of the electron distribution function and the enhanced cooling this causes. The elevated T_e increases the conductivities by reducing the local plasma recombination rate and therefore increases the plasma density *Gurevich* [1978]; *St Maurice* [1990]; *Dimant and Milikh* [2003]; *Milikh et al.* [2006].

The NC model was developed by *Oppenheim* [1996, 1997]. This predicts a non-linear current driven by FB turbulence in the direction of the DC field. The model used in the MIX module combines $E_{\text{Thr}}^{\min}(E)$ with an assumed level of saturated FB instabilty density fluctuations as seen in simulations by *Oppenheim and Dimant* [2013]. This modifies the Hall and Pedersen conductance, as described in *Dimant and Oppenheim* [2011b].

Both AEH and the NC predict enhanced conductivities at all locations where turbulence exists. For use in LFM, these must be integrated along magnetic field lines to give conductances. That requires knowing the undisturbed plasma densities and collision rates throughout the turbulent region. This research applies simple averaged ionospheric plasma density profiles and collision frequencies from *Gurevich* [1978]. These averaged models are only needed to mimic typical altitude distributions of these quantities in order to calculate simple turbulent correction factors to the laminar conductances. The laminar conductances themselves are calculated within the MIX module, as described in Section 2.1. A more accurate and self-consistent model for the non-linear conductances using more accurate local altitudinal profiles will be implemented in the framework of the combined LFM-TIEGCM-MIX (CMIT) model.

Inside the MIX module we have implemented the following conductance correction terms combing the AEH and NC correction factors. In regions where the electric field is greater than 35 mV/m we have implemented,

$$\Sigma_P^{ET} = \Sigma_P^O(1 + 0.01(E - 35) + 1.3e \cdot 10^{-5}(E - 35)^2), \tag{1}$$

as the calculation for the (ET) modified conductance, Σ_P^{ET}. In Equation 1 E is the ionospheric electric field in mV/m and Σ_P^O is the Pedersen conductance obtained from the baseline ionospheric model and includes both the EUV and electron precipitation terms. This multiplier includes the effect of the temperature driven recombination reduction as well as the that of non-linear current. The ET modified Hall conductance, Σ_H^{ET} , is simply

$$\Sigma_H^{ET} = \Sigma_H^O(1 + 0.01172(E - 35) - 1.207e \cdot 10^{-5}(E - 35)^2), \qquad (2)$$

where Σ_H^O is the baseline Hall conductance. Figure 1 shows the effects of these multipliers over a range electric fields. The Pedersen multiplier (blue curve) is nearly linear over the range from 35-200 mV/m reaching a peak value of 3.0 at 200 mV/m. The Hall multiplier has a negative coefficient on the the squared term and so falls off more dramatically at higher values of the electric field. It reaches a value of 2.3 at 200 mV/m. We note that the FB Instability typically starts developing if the convection field, E, exceeds ≈ 20 mV/m. However, the macroscopic effect of E-region turbulence becomes substantial only for field when it exceeds $E > 35$ mV/m, therefore we eliminate the effect below this level for computational simplicity.

2.3 17 March 2013 Simulation

On 17 March 2013 an interplanetary coronal mass ejection arrived at the Earth and drove a significant geomagnetic storm, $D_{ST} < -100$, over the next day. Solar wind conditions obtained from the OMNI dataset were used to drive the LFM-RCM model and those are shown in Figure 2. Prior to the shock preceding the CME, the solar wind conditions are fairly typical, namely density ≈ 5 per cc, velocity ≈ 425 km/s, with interplanetary magnetic field (IMF) weak, < 5nT in magnitude, mainly in the northward direction. At 05:55 UT a shock is clearly present in the solar wind with V_X GSM reaching -650 km/s and the density increasing to 10 per cc. In the next three hours the IMF is variable, with IMF B_Z mainly southward reaching values of -20 nT, but having significant intervals with northward IMF. The Y component of the IMF has similar magnitude in amplitude and appears to have a 180 deg phase shift. After approximately 09:00 UT on the 17th the Y and Z components become more in phase and slowly reduce in amplitude reaching typical values by the end of the day. After about 12:00 UT the solar wind speed slowly begins to decrease reaching a value of about 550 km/s by the end of 17 March.

The LFM-RCM simulations for this interval where run using solar wind conditions from Figure 2. As previously discussed the LFM uses a non-orthogonal spherical mesh for the grid. The simulations conducted here use 106 radial, 96 azimuthal, and 128 polar cells. This quad resolution version of the LFM contains twice as many cells in each dimension as the results reported by *Pembroke et al.* [2012] initial work with coupling LFM-RCM. The RCM simulations where done on a grid with 200 cells in latitude and 100 cells in longitude and 90 energy channels (28 electron channels, 62 ion (H+) channels). The intermediate transfer grid between LFM-RCM used for the field line tracing had a size of 117 x110 x110 (x,y,z) points. In the MIX ionospheric solution the ionospheric resolution was increased from a $2x2°$ resolution to $1x1°$ resolution. The full ionospheric conductance model described by *Wiltberger et al.* [2009] by was enabled in the MIX calculations. We ran two sets of simulations. The first hereafter, baseline, used the standard ionospheric model. The second, hereafter ET, had the Electrojet Turbulence implementation discussed in Section 2.2 enabled. The solar wind driving, grid resolution, and all other model parameters are not changed between these two runs.

3 Analysis of results

We now move on to presenting the results of from the two simulations for the St Patrick's Day 2013 storm event. We begin, in Section 3.1, with a broad overview of the results of the simulation including comparisons of ionospheric structures and global measures. After this overview of the event and simulation results, we move onto making comparisons between the simulation results and observations. In Section 3.2 we make detailed comparisons between the simulation
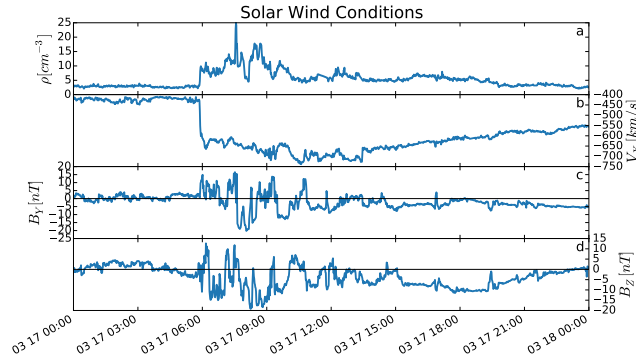
Figure 2. Solar wind and IMF conditions during the 17 March 2013 geomagnetic storm event. Panel a) shows the number density, b) the V_X in GSM coordinates. The IMF GSM Y and Z values are plotted in panels c) and d) respectively.

results and Defense Meteorological Satellite Program (DMSP) observations during the peak of the storm. These results show ability of the model capture features associated with Sub-Auroral Polarization Streams (SAPS). Next, we assess the ability of the model to simulate field aligned currents (FACs) by compare the results with patterns obtained from the AMPERE mission. Finally, in Section 3.4 we examine the structure of the inner magnetospheric pressures associated with the ring current by comparing the results with those derived from the TS07d empirical magnetic field model.

3.1 Baseline versus ET

Figure 3 is a frame extracted from the scientific visualization that is included in auxiliary materials that are part of the online version of this article. The top row figure shows the results from the baseline simulation while the bottom row shows the results from ET simulations. Panels a) and d) of Figure 3 provide a comparison between the cross polar cap potential patterns and the structure of the field aligned currents for the northern hemisphere during the course of the magnetic storm. In the snapshot taken at 10:00 UT on March 17th the region-1 and region-2 FAC current structures are clearly apparent. The cross polar cap potential is weaker in the ET run, but the alignment of the pattern in confinement to high-latitudes by the region-2 currents is consistent in both simulation results. The second column, panels b) and e), shows the Pedersen conductance. In both runs the EUV ionization profile is apparent on the dayside along with auroral oval structure driven by the empirical precipitation model. It is also clear at this snapshot that the ET model is having an impact because the Pedersen conductance in the auroral oval is larger in the ET results. The final column of Figure 3, panels c) and f), provides a comparison between the Hall conductances. Just like in Pedersen conductance the EUV profile and auroral oval are apparent in the Hall conductances. It is important to note that when comparing the conductance plots that color ranges are the same across simulations for each type of conductance, but the Hall conductance upper limit is a factor of two larger than the Pedersen conductance in order to make the differences between the results more apparent.

Before moving onto the examination of the evolution of the ionospheric parameters in the simulation during the course of the magnetic storm we turn our attention to Figure 4 that shows a comparison of several global diagnostic parameters over the course of the storm. The top panel, a), shows the time history of the cross polar cap potential obtained by taking the difference of the max and min of the potential at each dump step. Using a convention that will be maintained throughout this paper the baseline simulation results are shown with the green line and the ET simulation results are shown with the purple line. The second panel, b), of the figure shows the strength field-aligned current obtained by integrating the positive FAC over the northern hemi-
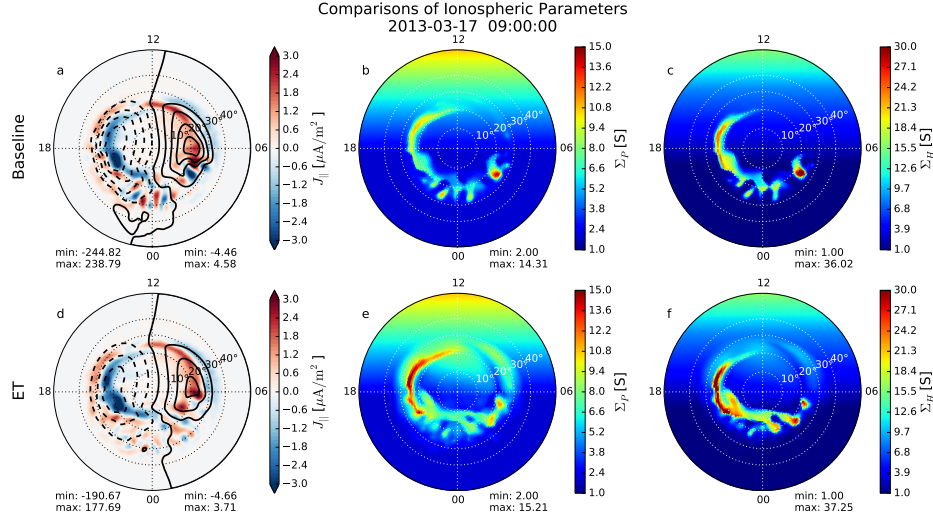
Figure 3. Frame from the scientific visualization showing of FAC and CPCP as well as Pedersen and Hall conductivities for the Baseline and ET simulations of the 17 March 2016 geomagnetic storm. The top row (panels a-c) contains the results from the baseline simulation while the bottom row (panels d-f) contains the results of the simulation with the ET enabled. The first column (panels a and d) has the FAC in color with blue being upward and red being downward as well as the CPCP pattern with 20 kV contours. The middle column (panels b and e) contains the Pedersen conductivity. The last column (panels c and f) contains the Hall conductivity. The color bar for the Pedersen conductance ranges from 1 to 15 [S] while the upper limit for the Hall conductance is 30 [S]

sphere at each time step. Panel c) at the bottom of Figure 4 shows a comparison between the simulation results and observations for the D_{ST} index. The simulated D_{ST} index was calculated using Biot-Savart method that determines the ground magnetic field perturbations driven by the magnetospheric, field-aligned, and ionospheric currents. Also shown in this panel is observed D_{ST} index obtained from CDAweb database. Following the convention for this paper the observed D_{ST} index is shown with a blue line.

The solar wind conditions prior to the 05:50 UT arrival of the shock preceding the CME are modest with velocity around 420 km/s, density slightly above 3 per cc and the IMF mainly northward with a small B_Y component. The scientific visualization of the ionospheric parameters begins at 00:00 UT on March 17th and results shown between then and the arrival of the shock show little difference between the two simulations. For example at 03:00 UT both simulations show a NBZ current system in the ionosphere with very weak convection patterns. There main conductance is coming from the EUV ionization and the maximum conductance values in both simulations are identical. In looking at the global diagnostic parameters plotted in Figure 4, the lines for the two simulations are virtually indistinguishable from each other during this interval. This is in line with our expectations that the ET affects will not be activated during typical solar wind conditions when the ionospheric electric field values are less then the 35 mV/m threshold.

After the arrival of the shock the speed exceeds 625 km/s with an initial period of strongly northward IMF followed by a roughly 40 minute interval of strongly southward IMF. Between 6:20 and 7:00 UT the IMF B_Z component is less than - 10 nT. Combined with the high solar speed, this leads to large cross polar cap potentials. The time history of CPCP and FAC in Figure 4 show for the first time significant differences in this interval. On average, the CPCP is 12.7 % smaller
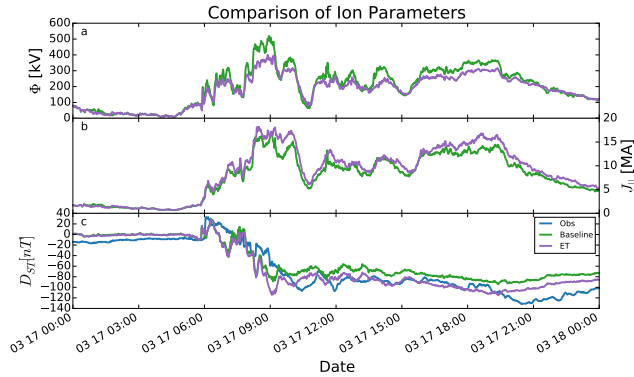
Figure 4. Comparison of the CPCP, FAC, and D_{ST} time series for the storm event for the Northern hemisphere. Panel a at the top shows the CPCP in kV. The middle panel (b) has the integrated FAC. Panel c at the bottom has the D_{ST} index. In each panel the LFM-RCM results are shown with the green line, the ET results with the purple line. In the bottom panel the D_{ST} obtained from CDAWeb is plotted in blue

in the ET run than the baseline simulation in this interval. This shows that the inclusion of the ET is having the intended effect of reducing the CPCP during strong driving conditions. During the same interval the FAC is 9.6 % larger in the ET run than the baseline simulation which is consistent with the more conducting ionosphere allowing stronger FAC currents [*Merkin et al.*, 2005a]. It also shows that there is tight coupling in magnetosphere-ionosphere system, so that one cannot consider the effects of changes in one region in isolation. Looking more closely at the scientific visualization at 07:00 UT, one sees that the most significant differences between the simulated conductances are occurring for the Hall conductance with maximum value 20 % higher in the ET run. This enhanced conductance occurs over the most of the auroral oval being most pronounced in the regions near midnight. It is worth pointing out that, while the CPCP and integrated FAC have significant differences, visual comparison of the FAC and CPCP patterns show considerable agreement between the location of the currents and the alignment of the convection pattern.

After this short period of southward IMF, the IMF turns northward and the disparity between the two simulations is reduced until the next interval of southward IMF arrives at 07:40 UT. With short excursions northward this period of strong driving lasts until roughly 10:00 UT. During the majority of this interval the IMF is typically less than -12 nT. Figure 3 shows the comparison between the baseline and ET runs at 09:00 UT which is in the middle of the interval of strong driving and corresponds to the largest difference between the CPCP seen in Figure 4. While there isn't much difference in the maximum in the Hall or Pedersen conductance at this time there is a clear and significant difference in the conductance patterns. The lack of difference between the maximum is due to the fact that the largest conductance in the baseline simulation is occurring in region just before dawn while the similar magnitude maximum is occurring throughout the dusk side in the ET results. The region of significant enhancement in conductance, roughly 3-4 [S] begins near 12 MLT and extends to 19 MLT. The high conductivity occurs approximately 15 degrees colatitude and maps to the region between the R1 and R2 currents evident in the FAC patterns. This corresponds to region of strong electric fields resulting from the current closure. This enhancement is evident in both the Pedersen and Hall conductance panels. Note that this is a qualitative improvement over the previous results by *Merkin et al.* [2005b] where no RCM coupling was implemented, and due to the lack of region 2 currents a larger portion of R1 currents closed over the polar cap. A similar enhancement of the conductance occurs in the pre-noon sector. It is occurring at lower latitudes, but still maps to the area between the R1 and R2 currents in that sector. There is also an enhancement of the conductance across 00 MLT occurring at high latitudes. It is worth noting that while the CPCP comes into rough agreement during the short
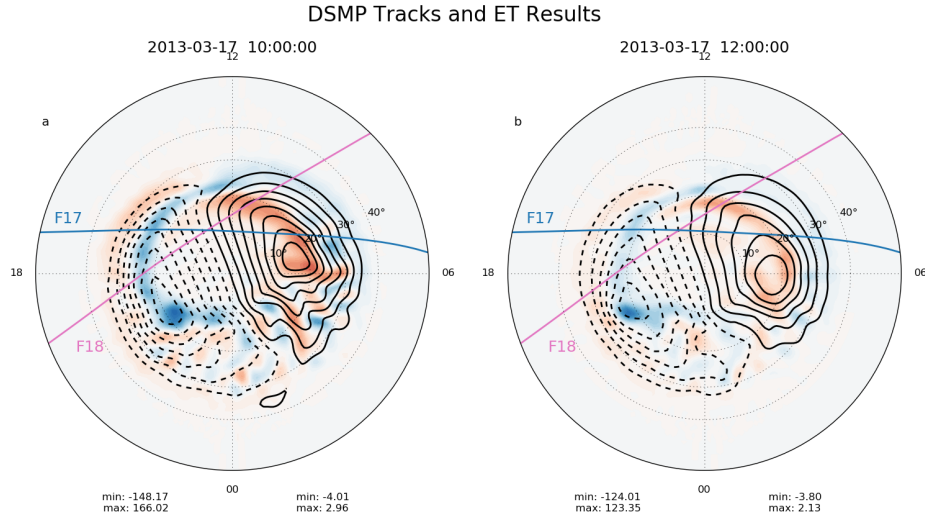
Figure 5. DSMP F17 and F18 trajectories overlaid on top of ET FAC and CPCP patterns. Panel a shows the F17 trajectory between 0945 and 1030 UT and the F18 trajectory between 1000 and 1045 UT overlaid on top of the ET simulation results for 10:00UT. Panel b shows the F17 trajectory between 1125 and 1210 UT and the F18 trajectory between 1145 and 1230 UT overlaid on top of the ET simulation results for 12:00UT. In each panel the F17 trajectory is blue and the F18 trajectory is pink.

northward excursion of the IMF the integrated FAC are different through and largest at the end of the interval.

As the storm progress throughout the remainder of the day on March 17th there are intervals during the CPCP in the ET run is significantly less than in the baseline simulation. Most notable of these are the periods 13:30-14:35 and 15:45-19:30 UT. Both intervals correspond to regions of southward IMF around -7 nT. In the first period the solar speed is near 700 km/s and in the second interval it declines from 625 to 600 km/s. Examination of the scientific visualization during these intervals reveals structures similar to those shown in Figure 3, especially in the enhancements on the dusk side and pre-noon sector between the R1 and R2 currents. It is also instructive to examine the ionospheric patterns at times when there is not a significant difference between the CPCP during the declining phase of the geomagnetic storm. At 13:26 UT, the CPCP and integrated FAC are nearly the same at 180 kV and 9 MA respectively. The conductance patterns are nearly the same as well with a 1 S difference in the maximum values and enhancement in the conductance in the pre- and post-noon sectors between the R1 and R2 currents.

As a final comparison between the two simulation results we turn our attention to the D_{ST} during the geomagnetic storm. Both simulations show positive enhancement of D_{ST} at the arrival of the shock. Between 06:20 and 08:30 UT the simulated D_{ST} indices follow roughly the same path of decreasing value. Both simulations reach a minimum D_{ST} value around 09 UT, but the ET value is 25 nT less than the value obtained by the baseline run. Both simulations reach the minimum value about 90 minutes before the observations. The 25 nT offset between the ET and baseline runs persists through the remainder of the storm. In the later phases of the storm the observed values come closest to the observations. While not shown here, it is worth pointing out as *Li et al.* [2016] did note that LFM-RCM simulations produce a significantly better agreement with D_{ST} than stand-alone LFM simulations.

3.2 Comparison with DMSP

So far the majority of results shown have only contrasted the two simulations. While this is instructive and illustrates the impact that the inclusion of the ET terms is having on the simulation results, it does not provide any verification as to whether the new results are in better agreement with observations. We begin this process by comparing the two simulation results with observations made by the DMSP spacecraft. Figure 5 shows the DMSP F17 and F18 trajectories during two intervals occurring in the main phase of the geomagnetic storm. The spacecraft were moving along the dusk-dawn meridian, measuring the horizontal component of ion drift velocity at altitude of approximately 830 km, together with fluxes of magnetospheric particle precipitation. The first pass occurring between 09:45 and 10:45 UT are at a time of significant difference between the two model results. During the second pass, 11:25 - 12:30 UT the difference between the simulation results is smaller.

The panels a and c of Figure 6 show comparisons on the cross-track ion drift velocity between the DMSP measurements and the two LFM-RCM simulations along two consecutive orbits of the F17 spacecraft over the northern hemisphere, orbiting from the duskside to dawnside across the polar region. The velocity shown in Figure 6 is perpendicular to the satellite trajectory, with negative values for anti-sunward convection and positive values for sunward convection. As indicated by the measured drift velocity in Figure 6, the DMSP F17 satellite passes through the regions of two-cell convection with sunward drift in the dusk sector, followed by anti-sunward drift over the polar cap and sunward drift in the dawn sector. Figures 6b and 6d show the corresponding energy flux of electron precipitation measured along the two DMSP F17 passes, respectively, together with the simulated energy flux of electron precipitation from the two LFM-RCM simulations. The measured equatorward boundaries of the auroral oval are indicated using blue dashed lines in each panel based on the sharp gradient in the measured electron energy flux. The green and purple dashed lines in Figure 6b and 6d indicate that the boundaries of the simulated auroral energy flux the spatial extension of the simulated auroral oval resembles the observations during the two F17 passes. According to the DMSP drift velocity and particle measurements, the observed double-channel profiles of the westward drift velocity on the dusk side (near 9:59 and 11:41 UT) are separated by the auroral precipitation boundary in both cases, indicating that the lower latitude westward plasma flow is in the subauroral region, which is also known as sub-auroral polarization streams (SAPS). The data-model comparisons suggest that both simulations are capable of reproducing the observed large-scale two-cell convection velocity profiles along the two consecutive DMSP F17 trajectories. It is clear that, with the ET switched on in the LFM-RCM simulation, the magnitude of the simulated velocity profiles along DMSP F17 passes is improved compared with the observed fast plasma flow in the subauroral region (during 09:54-10:00 and 11:34-11:40) where there is little electron precipitation flux.

A similar comparison between the LFM-RCM simulation and the measurements from two consecutive DMSP F18 passes during the main phase of the storm is shown in Figure 7. The data-model comparisons on the first F18 pass shown in Figure 7a suggest that with the ET module switched on, the LFM-RCM is capable of reproducing the double-channel convection profiles between 10:09-10:18. As indicated by the profile of the simulated auroral energy flux, the first peak occurs in the sub-auroral region while the second peak occurs at the location with peak auroral energy flux. The relative relationship between the distribution of the double-channel convection and the distribution of auroral energy flux is also seen in the DMSP F18 observations. Noticeable differences include the magnitudes of peak convection velocities and the location of the double-channels. Both the simulated double-channel convection profile and the precipitating electron energy flux profile along the F18 trajectory are approximately four to five degrees poleward compared to the corresponding measured profiles. The disagreement in the location of the auroral oval is likely a consequence of the fact that the distribution of upward Region 1 field-aligned currents in the global simulation is several degrees in MLAT poleward compared to observations [*Zhang et al.*, 2011]. Note that, on the dawnside, the LFM-RCM simulation misses the channels of anti-sunward flow observed by the two DMSP F18 passes near 10:27 and 12:12 UT, which is possibly due to the fact that the simulated high-latitude convection pattern in LFM-RCM is more contract than
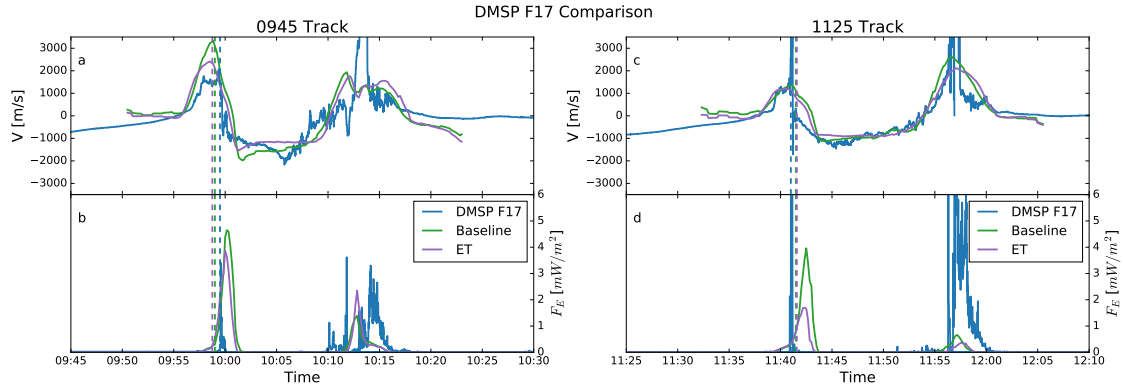
Figure 6. Comparison of DMSP F17 observations and simulation results. The first column, panels a and b, show the comparison for the 0945 pass. The second column, panels c and d, have the comparison for the 1125 pass. The first row, panels a and c, compare the cross track ion velocity from DMSP with the velocities obtained from the Baseline and ET simulations. The second row, panels b and d, compares the electron energy fluxes. In each panel the observations are show in blue, the baseline results in green and ET results in purple.
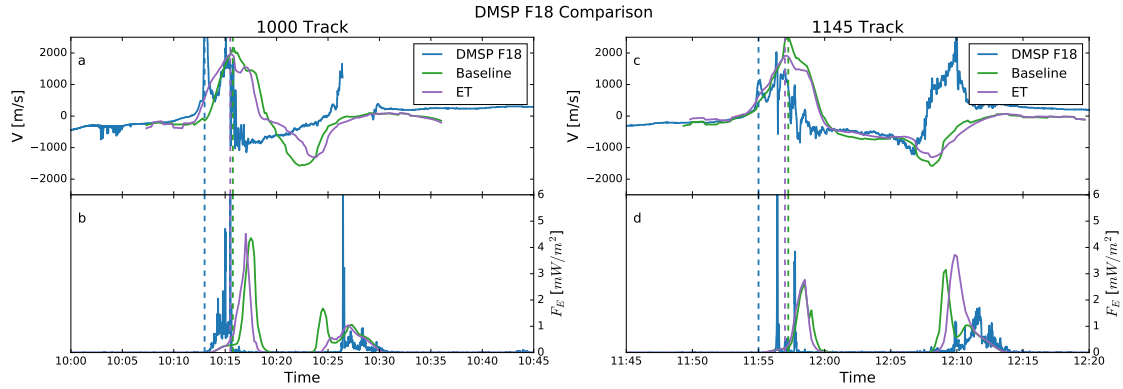

Figure 7. Comparison for DSMP F18 observations in the same format as Figure 6.

the measurements in the on the duskside. The comparisons on the second DMSP F18 pass between 11:55 and 12:00 is shown in Figure 7b. The simulated SAPS signature is approximately four degrees poleward compared to the measured one, which is similar to the comparison shown in Figure 7a. The comparisons between the two simulations suggest that, with the ET physics, the simulated convection velocity profile is improved with evident double-channel structures, although future investigations are necessary to further improve the model results.

3.3 Comparison with AMPERE

Now we move onto a comparison of the simulation results with the observations of the FAC patterns obtained from the AMPERE mission. The second scientific visualization accompanying this paper makes this comparison by plotting the patterns of the northern hemisphere currents along with cuts along specific MLTs. Figure 8 is extracted from this visualization at 09:00 UT on March 17th. The top row in the visualization provides a comparison of the FAC patterns for the northern hemisphere from the simulation and the AMPERE reconstruction. A two minute cadence was adopted for this visualization to match the highest output frequency available for the AMPERE observations. It is important to note that the AMPERE observations are built up over a 10 minute window and that accumulated pattern is being compared with an instantaneous
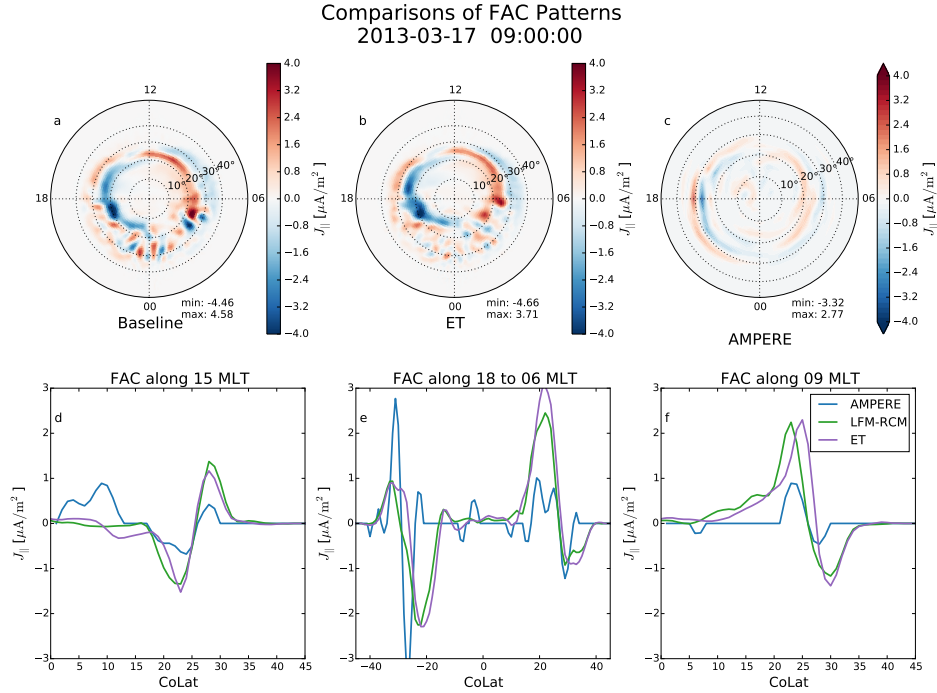
Figure 8. Frame extracted from the scientific visualization comparing the FAC from the simulations with the patterns derived from AMPERE magnetometer observations. The top row, panels a-c, shows the FAC patterns for the northern hemisphere using the same color bar. Panel a is the baseline simulation, panel b is the from the Electrojet Turbulence simulation and panel c is from the AMPERE observations. The bottom row makes comparisons of current strengths along cuts in MLT. Panel d is a cut along 15 MLT and extends from 0-45 degrees colatitude. Panel f is cut along 09 MLT and has the same range as panel a. Panel is a cut along the 18 and 06 MLT line. In this plot the negative colatitude values correspond to locations along the 18 MLT line, while the positive values are along the 06 MLT line. This plot gives a cut from dusk to dawn in a single panel. In all the comparison plots the AMPERE observations are shown in blue, the baseline simulation in green and the ET simulation in purple.

value obtain from the MIX output. In order to allow for a more quantitative comparison the bottom row of the visualization contains cuts from the current densities at several magnetic local times. Panels d and f provide cuts through the morning and afternoon sectors, while panel e provides a cut from dusk to dawn.

As discussed in Section 3.1, prior to the arrival of the shock the solar wind driving of the magnetosphere is quite weak. At 03:00 UT the solar IMF is mainly northward and a careful examination of the FAC patterns at this time shows an NBZ current system in both simulation results. The faint trace of an NBZ current system is apparent in the afternoon sector. These patterns can be hard to see in the visualization since the range of the color bar was selected to capture times when strong currents are flowing. Turning our attention to the MLT comparisons we see that for the 09 and 15 MLT cuts the two simulation results are virtually identical. Differences can be seen in the 18 MLT portion of the dawn-dusk cut, due the current in the ET version extending slightly more anti-sunward. The NBZ current systems do not appear in the AMPERE reconstruction, especially since a threshold value of 0.15 $\mu A m^{-2}$ is needed for the currents to above the noise threshold. The strong level agreement between the two simulations is not surprising since the ET effects are not likely to occur at this point in the simulation.

Next we focus our attention at 09:00 UT shown in Figure 8. It corresponds to time with the largest differences in CPCP seen between the two simulation results. While the difference between the CPCP is largest at this time, FAC patterns for the two simulations are similar, particularly on the dayside, in terms of their location, width, and strengths of the R1 and R2 current densities. There is a notable difference on the nightside, with the baseline simulation having stronger FAC pairs in the midnight sector. Also the peaks in the R1 currents that occur below the 18-06 MLT line are stronger in the baseline simulation. The strength of the currents is stronger than those seen in the AMPERE results. The R1 and R2 currents also appear to be at higher latitudes than those seen in the AMPERE results. The weaker current density in the AMPERE results has been reported before by *Merkin et al.* [2013] and can be partially explained by the fitting process underestimating the true current density. Looking at the 15 MLT comparison we see that the strength of currents along this cut is similar in the baseline and ET simulations. The current density peaks are higher and about a 1-2 degrees poleward of those in AMPERE. In the 09 MLT there is a 1-2 degree difference in the location of the peak current between the two simulation results. The current density peaks in the two simulations appear to bracket the observed current density peak with the baseline simulation peak at above the AMPERE peak and the ET peak below it. The peak current density here is about a factor of two larger than the AMPERE results and the current densities structures are wider. The wider current densities in the simulation results are also seen in the 18-06 MLT cut. This is especially clear for the current densities in the 18 MLT line. Unlike the other current densities reported here the AMPERE current densities are stronger in this region. Along the 06 MLT cut the current densities return to being about a factor of 2 larger in the R1 location. At this time CPCP differences between the simulations are largest, however the difference between the currents in the two simulations is relatively modest. Furthermore, both simulations agree quite well with the AMPERE observations.

As the storm progress through the remainder of the day, there are intervals with strong solar wind driving that result in significant differences in the simulated CPCP. The 14:00 UT frame is typical of the conditions seen during the 13:30-14:35 interval of strong driving. The modest 1-2 degree separation between the current peaks noted in the 09 MLT cut of the 09:00 UT results is present in all of the cuts through the currents. In general, the baseline simulation peak appears to be closer to the peak in the AMPERE observations then the ET simulation results. This trend is also apparent in the 15:45-19:30 UT interval of strong driving with the 16:12 frame providing a clear example. Also notable in this frame are the strong peaks in the R1 currents below the 18-06 MLT line in the ET simulation results. It is worth pointing out that at 13:26 UT time, previously identified as an instant with little differences between the CPCP and integrated FAC there are very small differences between the two simulation results.

3.4 Comparison with TS07d

In this final section we turn out focus our into the magnetosphere and make a comparison between the simulation results derived from the TS07d empirical magnetic field model model *Tsyganenko and Sitnov* [2007]; *Sitnov et al.* [2008]. TS07d differs from classic Tsyganenko magnetic field models [e.g., *Tsyganenko*, 1995]], because it presents the magnetic field of equatorial currents using a system of basis functions, whose number can be increased to improve the models ability to resolve progressively finer structures. This new reconstruction technique allowed for the first time to resolve the eastward ring current *Stephens et al.* [2016] near Earth, which is critical for correctly capturing the location and magnitude of the ring current pressure peak. The pressure reconstruction procedure using the isotropic force balance condition $\vec{J} \times \vec{B} = -\nabla P$ was described in detail by *Sergeev et al.* [1994] and then applied to reconstruct the pressure distributions on the basis of the TS07d by *Stephens et al.* [2016].

Figure 9 presents this comparison for the baseline (panel a) and ET (panel b) simulations with the TS07d (panel c) results for 16:00 UT on March 17th. The data are extracted from the SM equatorial plane and compared with the GSM equatorial in the TS07d results. At 16:00 UT the dipole tilt angle is only 8.4 degrees so the differences between these planes close to the Earth will be small. We selected 16:00 UT as the time for this comparison because it is well into the
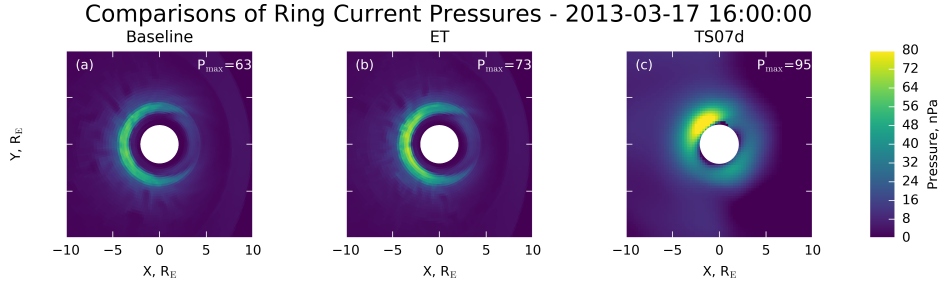
Figure 9. Inner magnetospheric pressures from simulations are compared with results from the TS07d empirical model. The panel on the left (a) shows the results from the baseline simulation, the middle panel (b) shows the ET simulations, and the right (c) shows the TS07d pressures. In each panel the peak pressure value is displayed in the upper right hand corner. All plots share the same color bar and view.

recovery phase of the geomagnetic storm when the ring current is well established. The white circle in the LFM-RCM plots represents the 2 R_E inner boundary location of the magnetospheric grid. We have also added a white circle panel c in order to facilitate visual comparison between the LFM-RCM results and those from the empirical model.

Visual comparison of the baseline and ET simulation results displayed in Figure 9 shows a similar shape and location of the inner magnetospheric pressure. The pressure is peaking inside of 4 R_E. A detailed examination of pressure along midnight, not shown here, indicates that the ET pressure peaks 0.2 R_E closer to the Earth than the baseline distribution. This difference is approximately the same as the inner magnetosphere cell sizes and is probably not significant. The peak pressure in the ET run is 10 nPa or 16 % higher than the baseline simulation. This difference is significant and is likely the source of better agreement with the observed D_{ST} index shown in panel c of Figure 4. The higher values for the peak pressure in the ET results are also improving the agreement with the peak pressures derived from the TS07d model.

Both of LFM-RCM simulation's pressure distributions are relatively symmetric about midnight. This is quite different from the the TS07d data shown in panel c which has peak in pressure in the pre-midnight sector. Along the midnight line a detailed examination of the pressure shows that it peaks at 2.9 R_E which is about 0.5 R_E closer to the Earth than the peak in either simulation result. Visual examination of the plots shows that the TS07d pressure distribution is more broad than either the baseline or ET simulations. In fact, looking again at the pressures along midnight we find that the width TS07d pressure at half the maximum value is 1.2 R_E or 50 % wider than either of the LFM-RCM simulation profiles. We do not yet understand what is driving these differences, but it is clear that the addition of the ET has not significantly impacted the shape of the inner magnetosphere pressures.

4 Discussion and Future Directions

In this work we have presented results from LFM-RCM simulations for a case study of a modest geomagnetic storm that occurred on 17 March 2013. These results include two significant changes to the LFM-RCM coupling than has been previously presented. First, are the infrastructure improvements to the LFM-RCM coupling methodology that allow it to deal with realistic solar wind conditions and dipole tilts. These changes place this version of the model on par with other models that couple global MHD simulations with the RCM and other ring current models. Second, we have implemented an electrojet turbulence model for modifying the ionospheric conductance. Generally speaking this model parameterized kinetic physics process that are not possible to directly model in a global simulations and result in significantly higher conductances in regions of strong electric fields.

One common problem with LFM simulations in the past has been the high values of the cross polar cap potential, relative to observations [e.g., *Gordeev et al.*, 2015], during strong solar wind driving conditions. The inclusion of the ET model in the LFM-RCM coupling results in significant reductions, on the order of 10 %, in the CPCP during the strong driving conditions seen in 17 March 2013 geomagnetic storm. Even though the inclusion of ET into the simulation lowers the CPCP, it is clearly not sufficient to bring the simulated CPCP values to those observed [e.g., *Shepherd*, 2007]. Other sources of CPCP overestimation such as the representation of magnetic reconnection in the simulation will need to be considered. Equally, important the inclusion of the model does not results in changes to the CPCP during modest driving conditions. We see that the enhancements to the conductance occur in the regions between the R1 and R2 currents flowing between the magnetosphere and ionosphere. The improved representation of the R2 currents provided by the coupling with the RCM play an important role in both the location and magnitude of the ET effects.

Inclusion of the ET effects produced significant improvements with the agreement to DMSP observations. First, turning on the ET reduced the cross track velocities bring them closer to the values observed by DMSP. Second, and more importantly, the inclusion of ET effects allowed the velocity profiles to obtain a double peaked characteristic of SAPS. This agreement was most clear for structures in the afternoon sector. The complicated structures currents in pre-midnight sector make direct comparisons with the DMSP observations more challenging, but the SAPS structures are clearly present here as well. Note that the predicted SAPS in the ET LFM-RCM simulation along the DMSP F18 pass is at the correct physical location, i.e., equatorward of the simulated auroral oval as shown in Figure 7, although the measured location of SAPS is approximately four degrees equatorward in magnetic latitude in the pre-midnight sector compared to the the simulated SAPS. It is possible that this discrepancy is a consequence of using an under-inflated background magnetic field model as previously explained by *Burke et al.* [1998], which is a dipole field in the LFM-RCM simulation. Moreover, the dynamics of storm-time ionospheric outflow may also play an important role in generating more realistic magnetic field topology especially in the plasmasheet [*Brambles et al.*, 2013], which is not included in the current LFM-RCM simulations.

In comparing the results of the simulations with field-aligned current observations made by AMPERE we note minor differences between the two simulation results for the FAC magnitudes and patterns. In fact, during the peak of the initial strong driving interval the strength and location of the peaks of the R1 and R2 currents are not significantly different from each other even though there is a difference in the cross polar cap potential at this time. The lower CPCP in the ET results is due to the increased ionospheric conductance and the magnetosphere acting close to a constant current source at this time. The response of the MI coupled system is not linear such that the longer the interval of strong driving lasts the greater the difference between the currents, with the ET simulation having higher integrated current values. We have not focused heavily on the comparison of currents on the nightside since both simulations show more structure in the FAC patterns than can be gleaned from the AMPERE fit to the data.

The comparison with the inner magnetosphere pressures shows little differences in terms of the structure or widths of the ring current pressure distribution in the inner magnetosphere. The ET simulation did have a 16 % higher peak pressure which was closer to the values derived from the TS07d model. In the simulation results the ring current pressure was rather symmetric with a peak near midnight, while the TS07d model pressure has a pre-midnight peak. The comparison presented in this paper is a preliminary effort in the direction of what we view as a very powerful tool for validation of global models. Inner magnetosphere pressure is a quantity that is very important for inferring the global state of the storm-time magnetosphere, since it regulates the generation of R2 currents and inflation of the geomagnetic field. At the same time, recovering its global distribution and, in particular, the location of the pressure peak is difficult from in situ data [e.g., *Gkioulidou et al.*, 2014] whereas global reconstructions, e.g., from energetic neutral atom (ENA) images [*Brandt, P. C.:Son et al.*, 2002] lack resolution and have substantial uncertainties. Thus, the empirical pressure reconstruction promises to be a highly useful tool for not

only validation, but also potentially adjustment, of inner magnetosphere pressures in global models. However, these reconstructions should first also undergo validation using in situ measurements and then much more detailed comparisons with global MHD simulations should be undertaken. We defer such a detailed analysis to a dedicated publication.

These initial results from the extension of the LFM-RCM show good agreement with a range of observations and notable improvements when the ET driven enhancements to ionospheric conductivity are included. They also point to several interesting directions for more detailed analysis. The capturing of the SAPS structures needs to be examined in more detail across a broader range of driving conditions. Particular attention needs to be paid to investigating what regulates when and where these structures are seen in the simulation results. Future investigations are needed to establish a system level understanding on the SAPS phenomenon using the coupld LFM-RCM model, including incorporating the feedback effect from ionospheric plasma chemical processes and thermospheric neutral dynamics using the fully coupled LFM-RCM-TIEGCM code. The evolution of the ring current pressures over this and other storms also requires more investigation. In particular, it is important to understand what determines the radial extent of the pressure distribution in the simulation as well as the radial and azimuthal location of the pressure peak.

Finally, as noted above, our ultimate goal in this project is to combine the work using LFM-RCM simulations presented here with the modeling that includes ET effects in the simulations of ionosphere-thermosphere self-consistently [*Liu et al.*, 2016]. This work is currently underway and will be presented in a future publication.

References

Bahcivan, H. (2007), Plasma wave heating during extreme electric fields in the high-latitude E region, *Geophysical Research Letters*, *34*(1), L15,106.

Balsley, B. B., and D. T. Farley (1971), Radar studies of the equatorial electrojet at three frequencies, *Journal of Geophysical Research*, *76*(3), 8341–8351.

Brambles, O. J., W. Lotko, B. Zhang, J. Ouellette, J. Lyon, and M. Wiltberger (2013), The effects of ionospheric outflow on ICME and SIR driven sawtooth events, *J. Geophys. Res.*, *118*(1), 6026–6041.

Brandt, P. C.:Son, D. G. Mitchell, Y. Ebihara, B. R. Sandel, E. C. Roelof, J. L. Burch, and R. Demajistre (2002), Global IMAGE/HENA observations of the ring current: Examples of rapid response to IMF and ring current-plasmasphere interaction, *J. Geophys. Res.*, *107*(A), 1359.

Buchert, S. C., T. Hagfors, and J. F. McKenzie (2006), Effect of electrojet irregularities on DC current flow, *Journal of Geophysical Research: Space Physics (1978–2012)*, *111*(A2), A02,305.

Buneman, O. (1963), Excitation of Field Aligned Sound Waves by Electron Streams, *Phys. Rev. Lett.*, *10*(7), 285–287.

Burke, W. J., et al. (1998), Electrodynamics of the inner magnetosphere observed in the dusk sector by CRRES and DMSP during the magnetic storm of June 4-6, 1991, *Journal of Geophysical Research*, *103*(A), 29,399–29,418.

Cohen, R., and K. L. Bowles (1967), Secondary irregularities in the equatorial electrojet, *Journal of Geophysical Research*, *72*(3), 885–894.

Coroniti, F. V., and C. F. Kennel (1973), Can the Ionosphere Regulate Magnetospheric Convection?, *J. Geophys. Res.*, *78*(16), 2837–2851.

Crochet, M., C. Hanuise, and P. Broche (1979), HF radar studies of two-stream instability during an equatorial counter-electrojet, *Journal of Geophysical Research*, *84*(A9), 5223–5233.

De Zeeuw, D. L., S. Sazykin, R. A. Wolf, T. I. Gombosi, A. J. Ridley, and G. Tóth (2004), Coupling of a global MHD code and an inner magnetospheric model: Initial results, *J. Geophys. Res.*, *109*(A), 12,219.

Dimant, Y. S., and G. M. Milikh (2003), Model of anomalous electron heating in the E region: 1. Basic theory, *Journal of Geophysical Research*, *108*(A), 1350.

Dimant, Y. S., and M. M. Oppenheim (2011a), Magnetosphere-ionosphere coupling through E region turbulence: 1. Energy budget, *Journal of Geophysical Research*, *116*(A), A09,303–n/a.

Dimant, Y. S., and M. M. Oppenheim (2011b), Magnetosphere-ionosphere coupling through E region turbulence: 2. Anomalous conductivities and frictional heating, *Journal of Geophysical Research*, *116*(A), A09,304–n/a.

Dimant, Y. S., and M. M. Oppenheim (2011c), Magnetosphere-ionosphere coupling through E region turbulence: 1. Energy budget, *Journal of Geophysical Research: Space Physics (1978–2012)*, *116*(A9), n/a–n/a.

Dimant, Y. S., and M. M. Oppenheim (2011d), Magnetosphere-ionosphere coupling through E region turbulence: 2. Anomalous conductivities and frictional heating, *Journal of Geophysical Research: Space Physics (1978–2012)*, *116*(A9), n/a–n/a.

Farley, D. T. J. (1963), A Plasma Instability Resulting in Field-Aligned Irregularities in the Ionosphere, *Journal of Geophysical Research*, *68*(22), 6083–.

Fedder, J. A., J. G. Lyon, S. P. Slinker, and C. M. Mobarry (1995a), Topological structure of the magnetotail as a function of interplanetary magnetic field direction, *J. Geophys. Res.*, *100*(A3), 3613–3621.

Fedder, J. A., S. P. Slinker, J. G. Lyon, and R. D. Elphinstone (1995b), Global numerical simulation of the growth phase and the expansion onset for a substorm observed by Viking, *Journal of Geophysical Research*, *100*(A), 19,083–19,094.

Foster, J. C., and P. J. Erickson (2000), Simultaneous observations of E-region coherent backscatter and electric field amplitude at F-region heights with the Millstone Hill UHF radar, *Geophys Res Lett*.

Fukao, S., M. Yamamoto, R. T. Tsunoda, H. Hayakawa, and T. Mukai (1998), The SEEK (Sporadic-E Experiment over Kyushu) Campaign, *Geophysical Research Letters*, *25*(11), 1761–1764.

Gallagher, D. L., P. D. Craven, and R. H. Comfort (2000), Global core plasma model, *J. Geophys. Res.*, *105*, 18,819.

Gkioulidou, M., A. Y. Ukhorskiy, D. G. Mitchell, T. Sotirelis, B. H. Mauk, and L. J. Lanzerotti (2014), The role of small-scale ion injections in the buildup of Earth's ring current pressure: Van Allen Probes observations of the 17 March 2013 storm, *J. Geophys. Res.*, *119*(9), 7327–7342.

Goodrich, C. C., A. L. Sussman, J. G. Lyon, M. A. Shay, and P. A. Cassak (2004), The CISM code coupling strategy, *J. Atmos. Solar Terr. Phys.*, *66*(1), 1469–1479.

Gordeev, E., et al. (2015), Assessing the performance of community-available global MHD models using key system parameters and empirical relationships, *Space Weather*, *13*(1), 868–884.

Gurevich, A. V. (1978), Nonlinear phenomena in the ionosphere, *New York*, *10*.

Hapgood, M. A. (1992), Space physics coordinate transformations - A user guide, *Planetary and Space Science (ISSN 0032-0633)*, *40*, 711–717.

Hill, T. W., A. J. Dessler, and R. A. Wolf (1976), Mercury and Mars - The role of ionospheric conductivity in the acceleration of magnetospheric particles, *Geophysical Research Letters*, *3*(8), 429–432.

Janhunen, P. (1996), GUMICS-3 A Global Ionosphere-Magnetosphere Coupling Simulation with High Ionospheric Resolution, *Environment Modelling for Space-based Applications*, *392*, 233.

Kelley, M. C. (1989), *The Earth's ionosphere*, Int. Geophys. Ser.

Kudeki, E., B. G. Fejer, D. T. Farley, and C. Hanuise (1987), The Condor Equatorial Electrojet Campaign: Radar results, *J. Geophys. Res.*, *92*(A12), 13,561.

Li, Z., M. Hudson, J. Paral, M. Wiltberger, and D. Turner (2016), Global ULF wave analysis of radial diffusion coefficients using a global MHD model for the 17 March 2015 storm, *J. Geophys. Res.*

Liu, J., W. Wang, M. Oppenheim, Y. Dimant, M. Wiltberger, and S. Merkin (2016), Anomalous electron heating effects on the E region ionosphere in TIEGCM, *Geophysical Research Letters*, *43*(6), 2351–2358.

Merkin, V. G., and J. G. Lyon (2010), Effects of the low-latitude ionospheric boundary condition on the global magnetosphere, *J. Geophys. Res.*, *115*(A), 10,202.

Merkin, V. G., A. S. Sharma, K. Papadopoulos, G. Milikh, J. Lyon, and C. Goodrich (2005a), Global MHD simulations of the strongly driven magnetosphere: Modeling of the transpolar potential saturation, *J. Geophys. Res.*, *110*(A), 9203.

Merkin, V. G., G. Milikh, K. Papadopoulos, J. Lyon, Y. S. Dimant, A. S. Sharma, C. Goodrich, and M. Wiltberger (2005b), Effect of anomalous electron heating on the transpolar potential in the LFM global MHD model, *Geophysical Research Letters*, *32*(2), 22,101.

Merkin, V. G., B. J. Anderson, J. G. Lyon, H. Korth, M. Wiltberger, and T. Motoba (2013), Global evolution of Birkeland currents on 10 min timescales: MHD simulations and observations, *J. Geophys. Res.*, *118*(8), 4977–4997.

Merkine, V. G., K. Papadopoulos, G. Milikh, A. S. Sharma, X. Shao, J. Lyon, and C. Goodrich (2003), Effects of the solar wind electric field and ionospheric conductance on the cross polar cap potential: Results of global MHD modeling, *Geophysical Research Letters*, *30*(2), 2180.

Milikh, G. M., and Y. S. Dimant (2002), Kinetic model of electron heating by turbulent electric field in the E region, *Geophysical Research Letters*, *29*(12), 1575.

Milikh, G. M., and Y. S. Dimant (2003), Model of anomalous electron heating in the E region: 2. Detailed numerical modeling, *Journal of Geophysical Research: Space Physics (1978–2012)*, *108*(A9), 1351.

Milikh, G. M., L. Goncharenko, Y. S. Dimant, J. P. Thayer, and M. A. McCready (2006), Anomalous electron heating and its effect on the electron density in the auroral electrojet, *Geophysical Research Letters*, *33*(1), L13,809.

Moen, J., and A. Brekke (1993), The solar flux influence on quiet time conductances in the auroral ionosphere, *Geophysical Research Letters*, *20*, 971–974.

Ohtani, S., S. Wing, V. G. Merkin, and T. Higuchi (2014), Solar cycle dependence of nightside field-aligned currents: Effects of dayside ionospheric conductivity on the solar wind-magnetosphere-ionosphere coupling, *J. Geophys. Res.*, *119*(1), 322–334.

Oppenheim, M. (1996), A wave-driven nonlinear current in the E-region ionosphere, *Geophysical Research Letters*, *23*(2), 3333–3336.

Oppenheim, M. (1997), Evidence and effects of a wave-driven nonlinear current in the equatorial electrojet, *Annales Geophysicae*, *15*(7), 899–907.

Oppenheim, M. M., and Y. S. Dimant (2013), Kinetic simulations of 3-D Farley-Buneman turbulence and anomalous electron heating, *J. Geophys. Res.*, *118*(3), 1306–1318.

Pembroke, A., F. Toffoletto, S. Sazykin, M. Wiltberger, J. Lyon, V. Merkin, and P. Schmitt (2012), Initial results from a dynamic coupled magnetosphere-ionosphere-ring current model, *J. Geophys. Res.*, *117*(A2).

Pfaff, R. F., M. C. Kelley, E. Kudeki, B. G. Fejer, and K. D. Baker (1987), Electric field and plasma density measurements in the strongly driven daytime equatorial electrojet: 2. Two-stream waves, *Journal of Geophysical Research: Space Physics (1978–2012)*, *92*(A12), 13,597–13,612.

Providakes, J., D. T. Farley, B. G. Fejer, J. Sahr, W. E. Swartz, I. Häggström, A. Hedberg, and J. A. Nordling (1988), Observations of auroral E-region plasma waves and electron heating with EISCAT and a VHF radar interferometer, *Journal of Atmospheric and Terrestrial Physics*, *50*(4-5), 339,349–347,356.

Raeder, J. (2003), Global Magnetohydrodynamics – A Tutorial, in *Space Plasma Simulation*, edited by J.˜Büchner, C. T. Dum, and M. Scholer, Springer Verlag, Berlin Heidelberg New York.

Raeder, J., w. d. cramer, j. jensen, T. Fuller Rowell, N. Maruyama, F. Toffoletto, S. Sazykin, and H. Vo (), Sub-Auroral Polarization Streams: A complex interaction between the magnetosphere, ionosphere, and thermosphere, in *th Annual International Astrophysics Conference*.

Raeder, J., R. J. Walker, and M. Ashour-Abdalla (1995), The structure of the distant geomagnetic tail during long periods of northward IMF, *Geophysical Research Letters (ISSN 0094-8276)*, *22*(4), 349–352.

Raeder, J., et al. (2001), Global simulation of the Geospace Environment Modeling substorm challenge event, *J. Geophys. Res.*, *106*(A1), 381–395.

Rasmussen, C. E., R. W. Schunk, and V. B. Wickwar (1988), A photochemical equilibrium model for ionospheric conductivity, *J. Geophys. Res.*, *93*(A9), 9831–9840.

Richmond, A. D. (1992), Assimilative mapping of ionospheric electrodynamics, *Adv. Space Res.*, *12*(6), 59–68.

Ridley, A., T. Gombosi, and D. DeZeeuw (2004), Ionospheric control of the magnetosphere: conductance, *Ann. Geophys.*, *22*(2), 567–584.

Rogister, A., and E. Jamin (1975), two-dimensional nonlinear processes associated with 'type 1' irregularities in the equatorial electrojet, *Journal of Geophysical Research: Space Physics (1978–2012)*, *80*(13), 1820–1828.

Rose, G., et al. (1992), The ROSE project. Scientific objectives and discussion of first results, *Journal of Atmospheric and Terrestrial Physics*, *54*(6), 657–667.

Schlegel, K. (1982), Reduced effective recombination coefficient in the disturbed polar E-region, *Journal of Atmospheric and Terrestrial Physics*, *44*(2), 183–185.

Schlegel, K., and J. P. St Maurice (1981), Anomalous heating of the polar E region by unstable plasma waves 1. Observations, *Journal of Geophysical Research: Space Physics (1978–2012)*, *86*(A3), 1447–1452.

Sergeev, V. A., T. I. Pulkkinen, T. I. Pellinen, and N. A. Tsyganenko (1994), Hybird state of the tail mangetic configuration during steady convection events, *J. Geophys. Res.*, *99*(A12), 23–.

Shepherd, S. G. (2007), Polar cap potential saturation: Observations, theory, and modeling, *J. Atmos. Solar Terr. Phys.*, *69*(3), 234–248.

Siscoe, G., G. Erickson, B. Sonnerup, and N. Maynard (2002a), Hill model of transpolar potential saturation: Comparisons with MHD simulations, *J. Geophys. Res.*, *107*(A6), 1075.

Siscoe, G. L., N. U. Crooker, and K. D. Siebert (2002b), Transpolar potential saturation: Roles of region 1 current system and solar wind ram pressure, *J. Geophys. Res.*, *107*(A), 1321.

Sitnov, M. I., N. A. Tsyganenko, A. Y. Ukhorskiy, and P. C. Brandt (2008), Dynamical databased modeling of the storm-time geomagnetic field with enhanced spatial resolution, *J. Geophys. Res.*, *113*(A), A07,218–n/a.

St Maurice, J. P. (1990), Electron heating by plasma waves in the high latitude E-region and related effects - Theory, *COSPAR*, *10*(6), 239–249.

St Maurice, J. P., and R. Laher (1985), Are observed broadband plasma wave amplitudes large enough to explain the enhanced electron temperatures of the high-latitude E region?, *Journal of Geophysical Research: Space Physics (1978–2012)*, *90*(A3), 2843–2850.

Stauning, P., and J. K. Olesen (1989), Observations of the unstable plasma in the disturbed polar E-region, *Phys. Scr.*, *40*(3), 325–332.

Stephens, G. K., M. I. Sitnov, A. Y. Ukhorskiy, E. C. Roelof, N. A. Tsyganenko, and G. Le (2016), Empirical modeling of the storm time innermost magnetosphere using Van Allen Probes and THEMIS data: Eastward and banana currents, *J. Geophys. Res.*, *121*(1), 157–

170.

Toffoletto, F. R., S. Sazykin, R. W. Spiro, and R. A. Wolf (2003), Inner magnetosphere modeling with the Rice Convection Model, *Space Sci Rev*, *107*, 175–196.

Tsyganenko, N. A. (1995), Modeling the Earth's Magnetospheric Magnetic Field Confined Within a Realistic Magnetopause, *J. Geophys. Res.*, *100*, 5599.

Tsyganenko, N. A., and M. I. Sitnov (2007), Magnetospheric configurations from a high-resolution data-based magnetic field model, *Journal of Geophysical Research: Space Physics (1978–2012)*, *112*(A6), n/a–n/a.

Welling, D. T., and A. J. Ridley (2010), Validation of SWMF magnetic field and plasma, *Space Weather*, *8*(3), 03,002.

Wiltberger, M., R. S. Weigel, W. Lotko, and J. A. Fedder (2009), Modeling seasonal variations of auroral particle precipitation in a global-scale magnetosphere-ionosphere simulation, *J. Geophys. Res.*, *114*(A), 01,204.

Wolf, R. A. (1983), The quasi-static (slow-flow) region of the magnetosphere, in *Solar Terrestial Physics*, edited by R. L. Carovillano and J. M. Forbes, pp. 303–368, Hingham, Hingham, MA.

Zhang, B., W. Lotko, M. J. Wiltberger, O. J. Brambles, and P. A. Damiano (2011), A statistical study of magnetosphere-ionosphere coupling in the Lyon-Fedder-Mobarry global MHD model, *J. Atmos. Solar Terr. Phys.*, *73*(5), 686–702.